Journal of Catalysis 364 (2018) 415–425

Contents lists available at ScienceDirect

Journal of Catalysis

journal homepage: www.elsevier.com/locate/jcat

Catalytic thiophene oxidation by groups 4 and 5 framework-substituted zeolites with hydrogen peroxide: Mechanistic and spectroscopic evidence for the effects of metal Lewis acidity and solvent Lewis basicity

Daniel T. Bregante, Ami Y. Patel, Alayna M. Johnson, David W. Flaherty *

Department of Chemical and Biomolecular Engineering, University of Illinois Urbana-Champaign, Urbana, IL 61801, United States

ARTICLE INFO

Article history:
Received 16 March 2018
Revised 4 June 2018
Accepted 8 June 2018

Keywords:
Oxidative desulfurization
Lewis acid catalysis
Zeolite catalysis
Solvent effects
Competitive adsorption
Mayr nucleophilicity

ABSTRACT

Group 4 (Ti and Zr) and 5 (Nb and Ta) atoms substituted into the *BEA zeolite framework (M-BEA) irreversibly activate hydrogen peroxide (H_2O_2) and form pools of metal-hydroperoxide (M-OOH) and peroxide (M-(η^2-O_2)) intermediates active for the oxidation of 2,5-dimethylthiophene (C_6H_8S), a model reactant representative of organosulfur species in fossil reserves and chemical weapons. Sequential oxidation pathways convert C_6H_8S into 2,5-dimethylthiophene oxide (C_6H_8SO) and subsequently into 2,5-dimethylthiophene dioxide by oxidative dearomatization. Oxidation rates measured as functions of reactant concentrations together with in situ UV–vis spectra show that all M-BEA activate H_2O_2 to form pools of M-OOH and M-(η^2-O_2), which then react with either C_6H_8S or H_2O_2 to form the sulfoxide or to decompose into H_2O and O_2, respectively. Turnover rates for C_6H_8S oxidation and H_2O_2 decomposition both increase exponentially with the electron affinity of the active site, which is quantitatively probed via the adsorption enthalpy for deuterated acetonitrile to active sites. C_6H_8S oxidation rates depend also on the nucleophilicity of the solvent used, and rates decrease in the order acetonitrile > *p*-dioxane ~ acetone > ethanol ~ methanol. In situ UV–vis spectra show that highly nucleophilic solvent molecules compete effectively for active sites, inhibit H_2O_2 activation and formation of reactive M-OOH and M-(η^2-O_2) species, and give lower turnover rates. Consequently, this work shows that turnover rates for sulfoxidation are highest when highly electrophilic active sites (i.e., stronger Lewis acids) are paired with weakly nucleophilic solvents, which can guide the design of increasingly productive catalytic systems for sulfide oxidation.

1. Introduction

Fossil fuel reserves and chemical warfare agent stockpiles contain potentially harmful organosulfur compounds (OSCs) that must be captured and sequestered by adsorption or deactivated by chemical or catalytic methods. These compounds threaten human and environmental health [1], because they are toxic in their native form but also because they form noxious species (i.e., SO_x) upon combustion. Crude fossil fuels contain up to 5 wt% OSCs [2], which must be reduced below 15 ppm (i.e., <0.015 wt%) to comply with environmental regulations for diesel fuels in many countries [3]. Furthermore, the sulfur contents of hydrocarbon feedstocks impact environmental pollution [4] but also the corrosion of equipment [5] and the reactivity of catalysts in down-stream processes [6]. OSCs are frequently removed from fossil fuels by hydrodesulfurization (HDS), which reduces OSCs using molecular hydrogen to liberate hydrogen sulfide (H_2S) [7–10] that is captured by chemical separations (i.e., absorption) or treatment (to form elemental sulfur) [11]. Aromatic sulfur compounds (e.g., thiophenes) comprise the vast majority of OSCs within fossil fuel reserves [2]. Yet, many HDS catalysts (e.g., $CoMoS/Al_2O_3$) give low rates for the hydrodesulfurization of hindered thiophenes (e.g., 4,6-dimethyldibenzothiophene) because the steric bulk surrounding the sulfide moiety hinders coordination to the catalyst surface [12,13]. Consequently, reduction of these compounds requires long residence times and harsh process conditions (e.g., high temperatures, high H_2 pressures) that leads also to undesirable hydrogenolysis reactions that reduce fuel quality [14,15].

Alternatively, oxidative desulfurization (ODS) can chemically abate the OSCs that are present in crude fuels without cleaving C—C bonds in long-chain hydrocarbons [16]. Oxidation of the sulfide moiety in thiophenes using environmentally benign oxidants, such as hydrogen peroxide (H_2O_2), produces less-toxic sulfoxide or

* Corresponding author.
E-mail address: dwflhrty@illinois.edu (D.W. Flaherty).

https://doi.org/10.1016/j.jcat.2018.06.009
0021-9517/

sulfone products that are easily sequestered and analogous oxidations of many chemical warfare agents eliminates their bioactivity [17]. Multiple articles have reported the synthesis and evaluation of titanium silicalite (TS-1) [16,18–21], titania-silicates (TiO_2-SiO_2) [22–24], Ti-BEA [21,25–27], and other Ti-based catalysts [28,29] for the oxidation of thiophenes. For example, Corma and coworkers have shown that Ti-BEA and Ti-MCM-41 are both active for the oxidation of methylphenyl sulfide (0.1 M, 0.3 M H_2O_2, CH_3CN solvent, 313 K) [21], with Ti-BEA possessing greater rates for sulfoxidation than Ti-MCM-41. When methylphenyl sulfide was exchanged for isopentylmethyl sulfide Ti-MCM-41 possessed greater rates, which was attributed to slower diffusion through the smaller-pore Ti-BEA. Hulea et al. have shown that Ti-BEA and Ti-HMS (HMS = hexagonal mesoporous silica) catalyze the oxidation of benzothiophene and dibenzothiophene, both of which were shown to be too bulky to enter the pores of MFI and react with TS-1 [25]. Notably, Ti-BEA was shown to possess higher rates than Ti-HMS, which we presume to be related to stabilization of the bulky thiophenic transition states within the smaller-pore *BEA. Thornburg et al. have recently shown that niobium silicates (Nb-SiO_2) efficiently oxidize thioanisole and possess nearly perfect selectivity toward the formation of the corresponding sulfone [28]. The Nb-SiO_2 catalysts are also significantly more active for thioanisole oxidation than Ti- and Zr-SiO_2 at 318 K, which exhibit initial turnover rates of 9.0, 7.9, and 2.3 min^{-1}, respectively [24]. These trends differ markedly different form those for epoxidation catalysis on similar materials, where rates of cyclohexene and styrene epoxidation are greatest for Ti-incorporated BEA and Ti-SiO_2, followed by the Nb analogues [30–33]. Currently, the reasons for the differences in thiophene oxidation rates and selectivities are unknown but may be related to changes in the mechanism for oxidation or to differences in the electronic structure and coordination of the active sites. Overall, the literature lacks a detailed mechanism for the oxidation of substituted thiophenes or guiding principles for the design of improved groups 4 and 5 catalytic systems for sulfoxidation chemistry.

Here, we seek to explain how and why rates and selectivities for the oxidation of 2,5-dimethylthiophene (C_6H_8S) depend on the intrinsic properties of active sites formed by substituting group 4 or 5 transition metal atoms into the framework of zeolite *BEA (M-BEA). A combination of reaction rates measured as a function of the reactant concentrations, in conjunction with spectroscopic measurements acquired in situ, show that all M-BEA activate H_2O_2 and oxidize C_6H_8S through a series of equivalent elementary steps that utilize similar reactive species. Comparisons of turnover rates for C_6H_8S oxidation within different solvents show that conversion rates depend exponentially on the nucleophilicity of the solvent mixture, which is quantified using the Mayr nucleophilicity scale. UV–vis spectra of Ti-BEA contacted by H_2O_2 solutions in these different solvent mixtures show a concomitant decrease in the number of M-(O_2) intermediates and C_6H_8S oxidation rates, which suggests that competitive adsorption of these Lewis basic solvents to the Lewis acidic metal centers contributes to the decrease in rates. These comparisons show that thiophene oxidation depends sensitively on the Lewis acid-base interactions between the active sites and the solvent molecules. Finally, reaction rates for C_6H_8S oxidation and H_2O_2 decomposition increase with a similar functional dependence on the electron affinity of the active sites, which are quantitatively compared using the adsorption enthalpy of deuterated acetonitrile to Lewis acid sites. Consequently, the design of catalytic systems that maximize the electron affinity of the group 4 or 5 metal center and utilize weakly Lewis basic solvent system give greater turnover rates for ODS without sacrificing the selective use of the costly oxidant, H_2O_2.

2. Methods and materials characterization

2.1. Synthesis and characterization of M-BEA

Ti-, Nb-, and Ta-BEA catalysts were synthesized by the post-synthetic modification of NH_4^+-BEA, while Zr-BEA was prepared by solid-state ion exchange of NH_4^+-BEA [30,31,34–37] and is detailed in our previous reports [30–32]. In short, NH_4^+-BEA (Zeolyst, CP814E) was dealuminated by reflux in HNO_3 (20 mL g^{-1}; Macron Chemicals, 69–70%) to produce Si-BEA (Si:Al > 1400, determined by EDXRF). Ti-, Nb-, and Ta-BEA were synthesized by refluxing an appropriate amount of Si-BEA with the corresponding metal chloride ($TiCl_4$ (Sigma, 99%), $NbCl_5$ (Sigma, 99.9%), $TaCl_5$ (Sigma, 99%)) in either dichloromethane (for Ti) or isopropanol (for Nb and Ta; Fisher Chemicals). Solids were then recovered by rotary evaporation. Zr-BEA was produced by grinding Si-BEA with an appropriate amount of $Zr(OEt)_4$ (Alfa-Aesar, 99%) to form an intimate mixture. In all cases, recovered solids were treated in flowing air (100 cm^3 min^{-1}; Airgas, Ultra-zero grade) and were heated to 823 K at 2 K min^{-1} for 6 h, which produced bright white solids.

The metal contents (Table 1) of the M-BEA catalysts were quantified using energy dispersive X-ray fluorescence (EDXRF) spectroscopy. Briefly, 30–40 mg of sample was loaded into a polypropylene sample holder (1 cm diameter) that was sealed with ultralene film. These were then loaded into a spectrometer (Shimadzu, EDX-7000), whose sample chamber compartment was purged with He. One hundred scans were taken from 0 to 30 keV and the relative intensities of the fluorescence features for each element was used to determine the percent by mass of each element present.

The crystallinity of the M-BEA materials and differences in framework bond lengths before and after post-synthetic modification were determined using powder X-ray diffraction. Samples were finely ground and loaded (~60 mg) onto a polycarbonate holder, which was mounted into a diffractometer (Siemens/Bruker, D5000) with Cu Kα radiation (0.15418 nm). All X-ray diffractograms (Fig. S1) were collected under ambient conditions. X-ray diffractograms were smoothed using a finite Fourier transform with 10 points of fitting and the highest intensity was used to determine the positions of peak centers.

Optical band edge energies (E_g) were determined by extrapolation of the linear portion of the corresponding Tauc plot calculated from diffuse reflectance UV–vis spectra (Fig. S2). M-BEA samples were intimately combined in a 1:10 by weight ratio with magnesium oxide (MgO; Sigma, 99.995%) prior to analysis. Total reflectance spectra were collected at ambient conditions on a UV–vis-NIR spectrophotometer (Agilent, CARY 5) using pure MgO as a background.

The heat of adsorption for deuterated acetonitrile (CD_3CN; Cambridge Isotopes, 99.8% D atom) bound to the cationic framework transition metal atoms (ΔH_{CD_3CN}) is used as a quantitative measure

Table 1
Band edge energies, silicon-to-metal ratios, metal loadings, silicon-to-aluminum ratios, and heats of adsorption for CD_3CN coordinated to lewis acidic metal atoms for M-BEA catalysts used for catalytic rate measurements.

Sample	Band edge (eV)[a]	Si:M ratio[b]	Weight loading (wt. %)	Si:Al ratio[b]	ΔH_{CD3CN} (kJ mol^{-1})[c]
Ti-BEA	4.2	550	0.14	>1400	−31 ± 2
Zr-BEA	5.3	60	2.4	>1400	−12 ± 1
Nb-BEA	4.0	690	0.22	>1400	−20 ± 2
Ta-BEA	4.6	570	0.53	>1400	−16 ± 2

[a] Measured by diffuse reflectance UV–vis spectroscopy.
[b] Measured by energy dispersive X-ray fluorescence spectroscopy.
[c] Determined using van't Hoff analysis of infrared spectra.

of the difference in electron affinity between the Lewis acid sites of the M-BEA catalysts. Values of ΔH_{CD_3CN} were determined using van't Hoff analysis of the coverage of CD_3CN, which was determined using infrared spectra. Catalysts were pressed into self-supporting wafers (~70 mg) and loaded into a custom-built transmission cell using CaF_2 windows [38], which was placed into a spectrometer (Bruker, Tensor 37) and connected to a gas manifold. M-BEA pellets were first heated to 423 K at 10 K min^{-1} and held for 1.5 h under flowing He (50 cm^3 min^{-1}; Airgas, Ultra-zero grade) with the intent to desorb water and other volatile species present. A background spectrum (128 scans, 4 cm^{-1} resolution) was then recorded in flowing He (50 cm^3 min^{-1}). CD_3CN (1.6 μL min^{-1}) was then introduced via a syringe pump (KD Scientific, Legato 100) and vaporized in flowing He within the gas-transfer lines to produce a mixture containing 1.5 kPa CD_3CN in He. ΔH_{CD_3CN} were measured by measuring the change in the peak area for ν(C≡N) of CD_3CN bound to Lewis acid sites as a function of inverse temperature (1.5 kPa CD_3CN, 100 kPa He; Fig. S3).

2.2. Kinetics of 2,5-dimethylthiophene oxidation and H_2O_2 decomposition

Rates for 2,5-dimethylthiophene (C_6H_8S; Sigma, >99%) oxidation and H_2O_2 (Fisher Scientific, 30 wt% in H_2O) decomposition were measured within batch reactors (100 cm^3, three-neck round-bottom flasks). C_6H_8S and H_2O_2 were added to a solution of CH_3CN (Macron Chemicals, 99.8%), ethanol (C_2H_5OH; Decon Laboratory, 200 proof), *p*-dioxane ($C_4H_8O_2$; Avantor, ACS Reagent), dimethylsulfoxide ($(CH_3)_2SO$; Macron Chemicals, ACS grade), tetrahydrofuran (C_4H_8O; Sigma, ACS grade), acetone ($(CH_3)_2CO$; Sigma, ACS Reagent), decane ($C_{10}H_{22}$; Sigma, >99%), or methanol (CH_3OH; Macron, ACS grade), with benzene (Sigma, 99%, thiophene free; used as an internal standard for chromatographic analysis) and heated to the desired temperature (303–348 K) while stirring at 700 rpm. M-BEA catalysts were added to initiate the reaction and small aliquots of the reaction solution were extracted as a function of time through a 0.22 μm syringe filter that removed suspended catalyst, which prevented further reaction. The concentrations of the organic components within these aliquots were quantified via a GC equipped with a flame ionization detector (HP, 5890). The concentration of H_2O_2 in each aliquot was measured by colorimetric titration using an aqueous solution of $CuSO_4$ (8.3 mM; Fisher Chemicals, >98.6%), neocuproine (12 mM; Sigma-Aldrich, >98%), and ethanol (25% v/v). The concentration of H_2O_2 was calculated by comparison of the absorbance at 454 nm to calibrated standards, measured using a visible-light spectrophotometer (Spectronic, 20 Genesys). The product of triply-oxidized C_6H_8S (i.e., $C_6H_8SO_3$) was determining using high-resolution electron ionization mass spectrometry. Briefly, liquid samples were injected into a gas chromatograph (Agilent, 7890) and resolved chromatographic features were ionized in a mass spectrometer (Waters, GCT Premier) using electron ionization techniques to determine the relevant mass-to-charge (m/z^+) ratios. In all reported data, the carbon balance closed within 95% and the standard uncertainty for measured reaction rates was <10%.

Rates for the conversion of C_6H_8S and H_2O_2 were measured as functions of reactant concentrations, and all reported results were obtained at differential conversion (i.e., <5% conversion of the limiting reagent). Reported turnover rates on Ti-BEA, which provides the greatest turnover rates among the materials reported here, do not change with the loading of Ti atoms within the *BEA framework (Section S1.2), which satisfies the Madon-Boudart criterion [39]. Consequently, concentration gradients within the catalyst particles and artifacts due to mass transfer are negligible under the conditions of this investigation.

2.3. In situ UV–vis measurements

M-BEA samples were pressed into 7 mm diameter self-supporting pellets and loaded into a custom-built liquid flow cell equipped with cartridge heaters for temperature control. UV–vis spectra were obtained in situ using a 45° diffuse-reflectance probe (Avantes, solarization-resistant fibers) connected to a modular fiber-optic spectrometer (Avantes, AvaFast 2048) with a compact deuterium-halogen light source (Avantes, AvaLight-DHc). Liquid solutions were introduced using a high-performance liquid chromatography pump (Waters, 515). Background spectra were collected after flowing CH_3CN (1 cm^3 min^{-1}) over the samples for 1 h at 313 K prior to changing the liquid reservoir to vary the reaction conditions. Between switching solvents, the Ti-(O_2) intermediates were removed by flowing a solution of C_6H_8S in CH_3CN (0.01 M; 1 cm^3 min^{-1}) for 2 h at 333 K. Processes for peak smoothing are described in Section S2.

3. Results and discussion

3.1. Catalyst characterization

X-ray diffractograms (XRD) for all M-BEA catalysts (Fig. S1a) shows that all materials are *BEA-type zeolites and that the post-synthetic modifications did not significantly alter the zeolite structure [40]. Comparisons between the X-ray diffractograms for the dealuminated *BEA and M-BEA materials (Fig. S1b, Ti, Zr, Nb, and Ta metal loadings of 1.2, 2.4, 1.5, and 3.0 wt%, respectively) show that the diffraction peak assigned to the d_{302} spacing [41] shifts from 22.52° for dealuminated *BEA to lower values (22.42–22.45°) following treatments intended to substitute Ti, Zr, Nb, and Ta atoms into the framework. The observed shifts match prior reports [35,42,43] and reflect an expansion of the *BEA lattice, which confirms that the transition metal ions (e.g., Zr^{4+} or Nb^{5+}) occupy tetrahedral sites following the synthesis methods used here [44]. The average crystallite sizes for all *BEA catalysts are 145 ± 8 Å, which was calculated using the Scherrer equation with the d_{302} spacing XRD feature (Fig. S1a). This suggests that post-synthetic modification does not significantly reduce the average crystallite size of the *BEA framework. Moreover, post-synthetic modification of Al-BEA does not result in significant differences in the surface area or pore volumes of materials [37,45], such that any differences in reactivity (vide supra) are due to differences in the metal identity or solvent choice rather than consequences of varying confinement within the micropores.

Table 1 summarizes the weight loading of transition metal atoms in the M-BEA catalysts used for kinetic measurements, as measured by energy dispersive X-ray fluorescence (EDXRF). For Ti-, Nb-, and Ta-materials, M-BEA were made to result in ~0.1 (M atom) $(unit\ cell)^{-1}$ on average (i.e., Si/M ratios >500), with the intent to form predominantly equivalent M-atom sites and to minimize intraparticle concentration gradients. Zr-BEA was synthesized with a lower Si/Zr ratio (i.e., higher metal loading) that results in ~1 (M atom) $(unit\ cell)^{-1}$ in order to accurately measure the kinetics behind C_6H_8S ODS on this catalyst (Section 2.2), because the turnover rates measured were very low. In all cases, the post synthetic modification results in M-BEA catalysts with a large number of residual silanol nests (i.e., $(SiOH)_4$ groups), because only a small fraction of the Al atoms in the parent Al-BEA were replaced. These high silanol densities lead to highly hydrophilic materials, the catalytic properties of which may differ from analogous structures with hydrophobic pores, such as those synthesized within fluoride media [40].

In all cases, M-BEA materials possess a single prominent UV–vis absorbance feature (e.g., at 230 nm for Ta-BEA) that correspond to

a charge transfer from the 2p orbitals of oxygen to the valence orbitals of the transition metal (i.e., Ti, Nb, Ta, or Zr) in the *BEA framework [46]. The relatively large band gaps (Table 1) and absence of other observable features shoulders at higher wavelengths strongly suggests that the transition metal atoms within each M-BEA are highly disperse and that these materials contain little, if any, oligomeric or bulk oxide phases [47].

Fig. 1 shows infrared (IR) spectra of CD_3CN adsorbed on all M-BEA materials. All spectra of CD_3CN adsorbed on M-BEA catalysts show contain an absorbance feature at ~2274 cm^{-1} attributed to the ν(C≡N) of CD_3CN bound to SiOH groups within the *BEA framework [30–32,37,40]. Ti-, Nb-, and Ta-BEA possess also additional peaks at 2302, 2306, and 2312 cm^{-1}, respectively, which correspond to the ν(C≡N) mode of CD_3CN bound to these Lewis acidic metal centers [31,37]. In addition to the peak at ~2274 cm^{-1}, Zr-BEA possesses a second feature at 2296 cm^{-1} assigned to CD_3CN bound to Lewis acid sites and a third peak attributed to CD_3CN coordinate to Brønsted acidic open sites (i.e., $(SiO)_3Zr(OH)$) [31,36,48]. Adsorption enthalpies for CD_3CN bound to Lewis acidic metal atoms (ΔH_{CD_3CN}) in the M-BEA framework were used to quantify differences in the electron affinity of these active sites, which serves as a descriptor for Lewis acid strength. Table 1 summarizes values of ΔH_{CD_3CN} for all M-BEA and shows that Ti atoms in *BEA have the greatest electron affinity, followed by Nb, Ta, and Zr, which matches our previous report [31]. These comparisons suggest that the transition metal atoms within *BEA are electronically equivalent, as ΔH_{CD_3CN} is independent of metal loading (e.g., Ti-BEA with a Ti loading of 0.14 wt% and 1.2 wt% each possess values of ΔH_{CD_3CN} of -31 ± 2) [31].

Collectively, these data suggest that the post-synthetic modification of the commercially-available Al-BEA does not significantly change the structure of the *BEA framework, successfully incorporates group 4 and 5 metal atoms into the framework of *BEA, and that the electron affinities (i.e., ΔH_{CD_3CN}) differ with elemental identity.

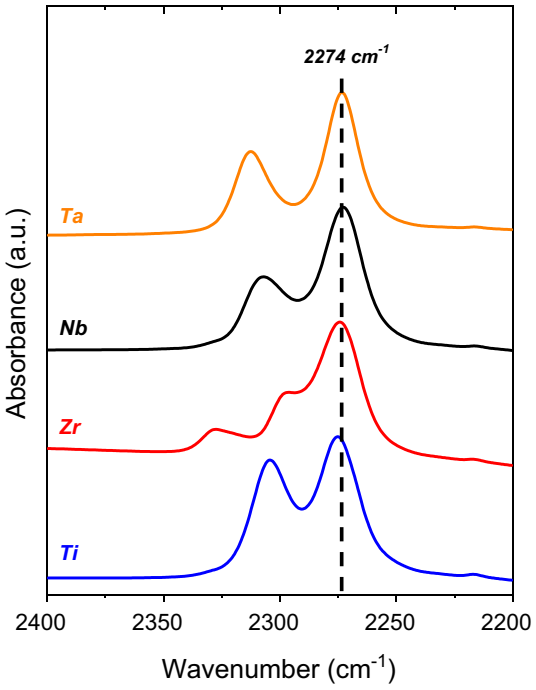

Fig. 1. Infrared spectra of CD_3CN bound to Ti-BEA (blue), Zr-BEA (red), Nb-BEA (black), and Ta-BEA (orange). Spectra were normalized to intensity of the ν(C≡N) mode of CD_3CN bound to silanol sites (2274 cm^{-1}) and were collected in flowing CD_3CN He (1.5 kPa CD_3CN, ~443 K).

3.2. Reaction pathways for the oxidation of 2,5-Dimethylthiophene

Fig. 2a shows the selectivity towards primary, secondary, and tertiary oxidation products as a function of 2,5-dimethylthiophene (C_6H_8S) conversion during the reaction of C_6H_8S with H_2O_2 over Ti-BEA (0.005 M C_6H_8S, 0.05 M H_2O_2, 313 K). The oxide (C_6H_8SO), 2,5-dimethylthiophene dioxide ($C_6H_8SO_2$), and $C_6H_8SO_3$ (e.g., epoxidized $C_6H_8SO_2$) as a function of C_6H_8S conversion over Ti-BEA (0.005 M C_6H_8S, 0.05 M H_2O_2, 313 K). As the conversion of C_6H_8S approaches zero, the selectivity towards 2,5-dimethylthiophene oxide (C_6H_8SO) nears 100%, which shows that C_6H_8SO is the sole primary product of C_6H_8S oxidation. The selectivity to 2,5-dimethylthiophene dioxide ($C_6H_8SO_2$) becomes detectable when the conversion exceeds 5% and reaches a maximum at ~40% conversion, which indicates that this sulfone forms by a secondary reaction. Selectivities to both the sulfoxide and sulfone products decrease as the C_6H_8S conversion increases, because tertiary reaction pathways also consume $C_6H_8SO_2$ to form the resultant 2,5-dimethylthiophene dioxide epoxide (i.e., $C_6H_8SO_3$; identified by mass spectrometry; m/z^+ = 160.0141) from oxidation of the C=C bonds within the thiophenic ring.

The selectivity patterns and reaction pathways of C_6H_8S oxidation differ markedly from oxidations of related sulfides (e.g., thioanisole) in which non-aromatic sulfide moieties readily oxidize to form the corresponding sulfone on Ti-based catalysts [49]. Specifically, singly-oxidized thiophenes (i.e., the corresponding sulfoxide) resist further oxidation [50]. Estimates using group

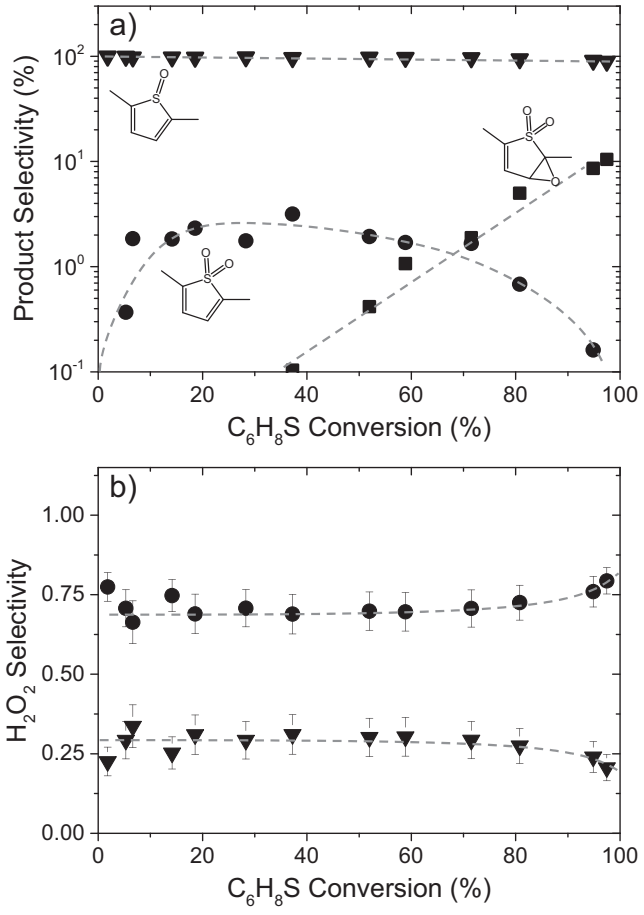

Fig. 2. (a) Product selectivity towards C_6H_8SO (▼), $C_6H_8SO_2$ (●), and oxidized $C_6H_8SO_2$ (■); and (b) selectivity for the consumption of H_2O_2 by oxidation reactions (▼) and H_2O_2 decomposition (●) as a function of C_6H_8S conversion (5 mM C_6H_8S, 0.05 M H_2O_2, 313 K) over Ti-BEA. Dashed curves are intended to guide the eye.

additivity indicate that the reaction enthalpy for the oxidation of C_6H_8SO to $C_6H_8SO_2$ is 37 ± 6 kJ mol^{-1} less exothermic than the initial sulfoxidation of C_6H_8S, because the second oxidation breaks the aromaticity of the ring [51]. Consequently, linear free energy relationships would suggest that barriers for oxidation of the sulfoxide would be greater than those for the thiophene, which is consistent with the change in selectivities with C_6H_8S conversion (Fig. 2a). The H_2O_2-mediated oxidation of C_6H_8S on Nb- and Ta-BEA catalysts shows similar product selectivity patterns (Fig. S6), which suggests that C_6H_8S reacts through identical reaction pathways that first form C_6H_8SO, which undergoes dearomative oxidation to form $C_6H_8SO_2$ and then $C_6H_8SO_3$ on all M-BEA. Fig. 2b shows the selectivity towards each of the two pathways for H_2O_2 consumption, thiophene oxidation and bimolecular H_2O_2 decomposition, as a function C_6H_8S conversion over Ti-BEA·H_2O_2 selectivities for thiophene oxidation remain constant (0.29 ± 0.06) at all values of C_6H_8S conversion. The H_2O_2 selectivities are nearly constant because the MASI changes throughout the course of the reaction due to competitive adsorption, which inhibits reaction rates of both C_6H_8S oxidation and H_2O decomposition pathways similarly.

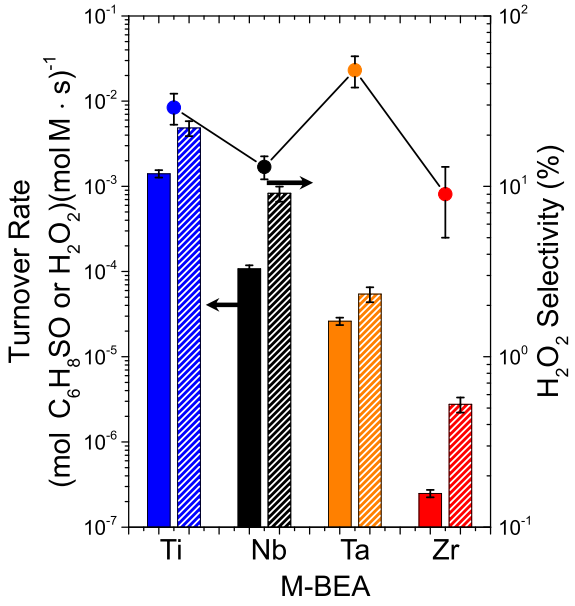

Fig. 3. Turnover rates for the formation of C_6H_8SO (solid bars), H_2O_2 decomposition (striped bars), and selectivities for H_2O_2 use in C_6H_8S oxidation (●, taken as a ratio of the turnover rate for C_6H_8SO formation to total H_2O_2 consumption, 0.01 M C_6H_8S, 0.01 M H_2O_2, 313 K) in CH_3CN as a function of metal identity in M-BEA.

Fig. 3 shows the turnover rates for C_6H_8S oxidation and H_2O_2 decomposition at differential conversion over all M-BEA catalysts at a standard set of conditions (0.01 M C_6H_8S, 0.01 M H_2O_2, 313 K). The rates of C_6H_8S oxidation and H_2O_2 decomposition vary significantly among the different M-BEA catalysts: Ti-BEA possesses rates for both pathways that are ~$3.5{\cdot}10^4$ times greater than those for Zr-BEA. Interestingly, the values of C_6H_8S oxidation and H_2O_2 decomposition rates tend to differ by similar amounts between the different metals; however, H_2O_2 selectivity does not follow the same trend as the turnover rates for C_6H_8S oxidation, as Ta-BEA possesses the highest selectivities at this set of conditions (~49%). Notably, Ta-BEA converts C_6H_8SO to $C_6H_8SO_2$ at lower C_6H_8S conversions than Ti-BEA (e.g., 10% versus 2% selectivity towards $C_6H_8SO_2$ for Ta-BEA and Ti-BEA, respectively at 20% C_6H_8S conversion; Fig. S6). These large differences in turnover rates and the lack of concomitant variance in H_2O_2 selectivities among these M-BEA catalysts clearly reflect some combination of differences between the specific surface species (i.e., most abundant surface intermediate) during C_6H_8S oxidation, the energetic barriers for each reaction pathway, or an intrinsic property of the active sites among the M-BEA catalyst, which are investigated in the following sections.

3.3. Kinetics and mechanistic interpretation of 2,5-dimethylthiophene oxidation

Fig. 4 shows initial turnover rates for the oxidation of C_6H_8S as a function of the concentrations of C_6H_8S, H_2O_2, and dimethylsulfoxide ($(CH_3)_2SO$; $(CH_3)_2SO$ was used as a model sulfoxide to measure the dependence of turnover rates on the concentration of initial sulfoxide product, because sufficiently pure samples of C_6H_8SO were not available) on Ti-, Nb-, Ta, and Zr-BEA catalysts. On these materials, relatively low ratios of the concentrations of C_6H_8S to that of H_2O_2 (e.g., $[C_6H_8S]:[H_2O_2] < 1$ on Ti-BEA) result in rates of

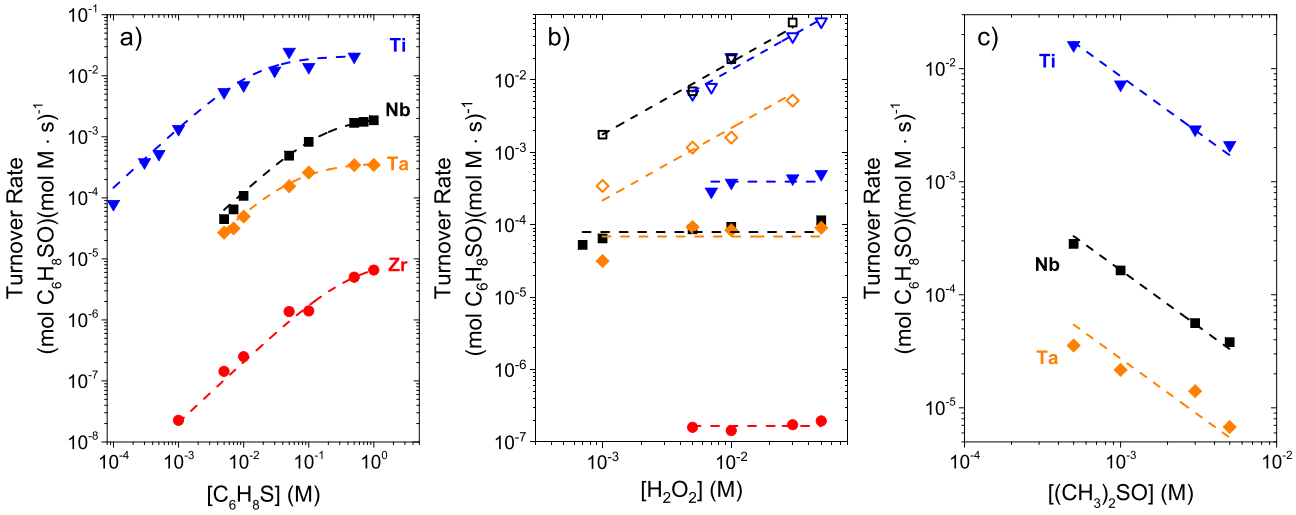

Fig. 4. Turnover rates for the formation of C_6H_8SO as a function of (a) $[C_6H_8S]$ for Ti-BEA (▼, 0.01 M H_2O_2), Nb-BEA (■, 1 mM H_2O_2), Ta-BEA (◆, 1 mM H_2O_2), and Zr-BEA (●, 0.01 M H_2O_2); (b) $[H_2O_2]$ for Ti-BEA (▼, 0.7 mM C_6H_8S; ▽ 0.5 M C_6H_8S), Nb-BEA (■, 7 mM C_6H_8S; □, 1 M C_6H_8S), Ta-BEA (◆, 7 mM C_6H_8S; ◇, 1 M C_6H_8S), and Zr-BEA (●, 5 mM C_6H_8S); and (c) $[(CH_3)_2SO]$ for Ti-BEA (▼, 0.01 M H_2O_2, 5 M C_6H_8S), Nb-BEA (■, 1 mM H_2O_2, 1 M C_6H_8S), and Ta-BEA (◆, 1 mM H_2O_2, 1 M C_6H_8S) at 313 K. Dashed lines represent least squares regression fits to the relevant equations in the main text (i.e., Eqs. (4), (6), and (8)).

C_6H_8S oxidation that increase linearly with $[C_6H_8S]$ and are not functions of $[H_2O_2]$, which suggests that active sites are saturated with H_2O_2-derived species under these conditions. As the $[C_6H_8S]$ increases further at constant $[H_2O_2]$, the rate of oxidation becomes independent of $[C_6H_8S]$, proportional to $[H_2O_2]$, and inversely proportional to $[(CH_3)_2SO]$, which shows that the most abundant surface intermediate (MASI) becomes a species formed from C_6H_8S (e.g., C_6H_8SO) [52].

Scheme 1 shows a series of elementary steps that account for the measured effects of $[C_6H_8S]$, $[H_2O_2]$, and $[(CH_3)_2SO]$ on sulfoxidation turnover rates across all M-BEA catalysts. The catalytic cycle for C_6H_8S oxidation involves the quasi-equilibrated adsorption of C_6H_8S (step 1) and H_2O_2 (step 2), followed by the irreversible activation of H_2O_2 (step 3) to form a pool of M-OOH and M-(η^2-O_2) intermediates [30–32], which are collectively denoted as M-(O_2). The active M-(O_2) species react with C_6H_8S (step 4) or C_6H_8SO (step 7) to form the corresponding sulfoxide or sulfone product, respectively, which then desorb (steps 6 and 8). Alternatively, the active M-(O_2) intermediates may decompose non-productively by reaction with liquid-phase H_2O_2 (step 5) [53]. Notably, the rate dependencies for this sulfoxidation on $[C_6H_8S]$ and $[H_2O_2]$ are analogous to the functional form of epoxidation rates on the concentrations of cyclohexene [31] and styrene [32] on M-BEA catalysts.

Rates of C_6H_8S oxidation (r_{Ox}) are equal to that for the kinetically relevant reaction of C_6H_8S with M-(O_2) intermediates, which takes the form:

$$r_{Ox} = k_4[M-(O_2)][C_6H_8S] \quad (1)$$

where k_x is the rate constant for step x in Scheme 1, and [M-(O_2)] is the number of active M-(O_2) intermediates. Application of the pseudo steady-state hypothesis (Section S5.1) to [M-(O_2)] transforms equation (1) to:

$$r_{Ox} = \frac{k_3k_4K_2[C_6H_8S][H_2O_2][*]}{k_4[C_6H_8S] + k_5[H_2O_2] + k_7[C_6H_8SO]} \quad (2)$$

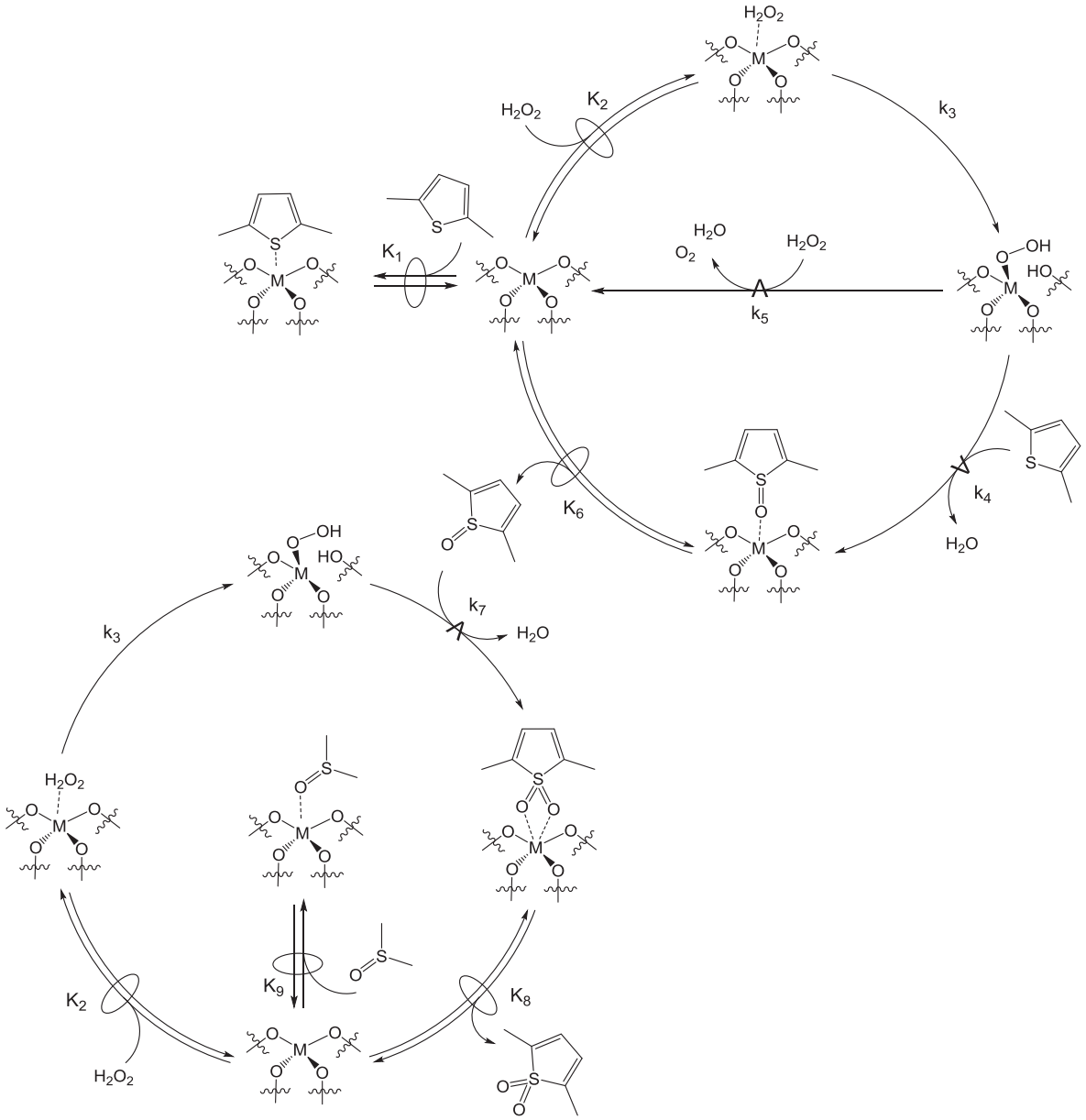

Scheme 1. Proposed Mechanism for the Oxidation of C_6H_8S and C_6H_8SO with H_2O_2 over M-BEA[a]. ([a]For brevity, only group 4 M-BEA (e.g., Ti- or Zr-BEA) closed sites are shown. The symbol ⇄ represents a quasi-equilibrated step, while → represents a kinetically relevant step. Note, the depiction of M-(O_2) and adsorbed C_6H_8S, C_6H_8SO, $C_6H_8SO_2$, $(CH_3)_2SO$, and H_2O_2 are meant to represent different types of surface species, rather than suggest a specific coordination to the active catalytic site).

where K_x is the equilibrium constant for step x in Scheme 1 and [*] is the number of unoccupied active sites that can bind to or react with specific species in solutions. An expression for [*] is given from the sum of all plausible surface intermediates

$$[L] = [*] + [M-(O_2)] + [C_6H_8S*] + [H_2O_2*] + [C_6H_8SO*] + [C_6H_8SO_2*] + [(CH_3)_2SO*] \quad (3)$$

where [L] is the total number of catalytically active metal atoms in the BEA framework, and [C_6H_8S*], [H_2O_2*], [C_6H_8SO*], [$C_6H_8SO_2$*], and [$(CH_3)_2SO$*] are the number of adsorbed molecules of C_6H_8S, H_2O_2, C_6H_8SO, $C_6H_8SO_2$, and $(CH_3)_2SO$, respectively. Finally, Eqs. (2) and (3) can be combined to yield a full rate expression for C_6H_8S oxidation

$$\frac{r_{Ox}}{[L]} = \frac{\frac{k_3 k_4 K_2 [C_6H_8S][H_2O_2]}{k_4[C_6H_8S]+k_5[H_2O_2]+k_7[C_6H_8SO]}}{\gamma} \quad (4)$$

where γ describes the sum of terms that represent all potential surface species.

$$\gamma = [1] + \frac{k_3 K_2 [H_2O_2]}{k_4[C_6H_8S] + k_5[H_2O_2] + k_7[C_6H_8SO]} + K_1[C_6H_8S] + K_2[H_2O_2] + K_6[C_6H_8SO] + K_8[C_6H_8SO_2] + K_9[(CH_3)_2SO] \quad (5)$$

such that the seven terms in γ correspond to the number of sites occupied by CH_3CN (i.e., the solvent), M-(O_2) intermediates, and adsorbed C_6H_8S, H_2O_2, C_6H_8SO, $C_6H_8SO_2$, and $(CH_3)_2SO$, respectively. At sufficiently low [C_6H_8S], and in the absence of $(CH_3)_2SO$, M-(O_2) intermediates become the MASI, which simplifies equation (4) to yield

$$\frac{r_{Ox}}{[L]} = k_4[C_6H_8S] \quad (6)$$

which is quantitatively consistent with rates of C_6H_8S oxidation that depend linearly on [C_6H_8S] (Fig. 4) and not on [H_2O_2] (Fig. 4). Similarly, at higher ratios of [C_6H_8S]:[H_2O_2] the oxidation products (e.g., C_6H_8SO) become the MASI, which appears as turnover rates that possess no dependence on [C_6H_8S] and increase proportionally to [H_2O_2]. When values of [C_6H_8S]:[H_2O_2] are large, the values of k_2[C_6H_8S] (C_6H_8S sulfoxidation) are much larger than for the terms k_4[H_2O_2] (H_2O_2 decomposition) and k_7[C_6H_8SO] (C_6H_8SO oxidation), because k_2 and k_4 are similar in magnitude and much larger than k_7 since C_6H_8SO resists oxidation [54]. This simplifies equation (4) to yield

$$\frac{r_{Ox}}{[L]} = \frac{k_3 K_2 [H_2O_2]}{K_6[C_6H_8SO]} \quad (7)$$

Eq. (7) matches the ways in which r_{Ox} change with [H_2O_2] and [C_6H_8S] (Fig. 4a and b). Changes in r_{Ox} as a function of [$(CH_3)_2SO$] were measured to emulate the effect of sulfoxide adsorption on rates, and the presence of $(CH_3)_2SO$* is accounted for by the form of the site balance in Eq. (5). Eq. (4) simplifies when $(CH_3)_2SO$* becomes the MASI (i.e., at high [C_6H_8S]) leading to:

$$\frac{r_{Ox}}{[L]} = \frac{k_3 K_2 [H_2O_2]}{K_9[(CH_3)_2SO]} \quad (8)$$

which resembles the observed dependence on [$(CH_3)_2SO$] on Ti-, Nb-, and Ta-BEA (Fig. 4). Rates of C_6H_8S oxidation on Zr-BEA were immeasurable ($<10^{-8}$ (mol C_6H_8SO) (mol M · s)$^{-1}$) in the presence of $(CH_3)_2SO$. The implied presence of high coverages of M-(O_2) intermediates and $(CH_3)_2SO$ on active sites under the ranges of reaction conditions discussed with Fig. 4 were probed directly by UV–vis spectra of M-BEA materials acquired in situ [53,55,56].

3.4. Effects of reactant concentrations and solvents on coverages of active species

UV–vis spectra collected in situ are needed to qualitatively determine the coverages of M-(O_2) and $(CH_3)_2SO$ surface species and to confirm the assumptions used to derive the rate expression for sulfoxidation (vide infra). Fig. 5 shows in situ UV–vis spectra of M-BEA catalysts during steady-state ODS at two relevant limits of reaction conditions: high ratios of [H_2O_2] to [C_6H_8S] that are

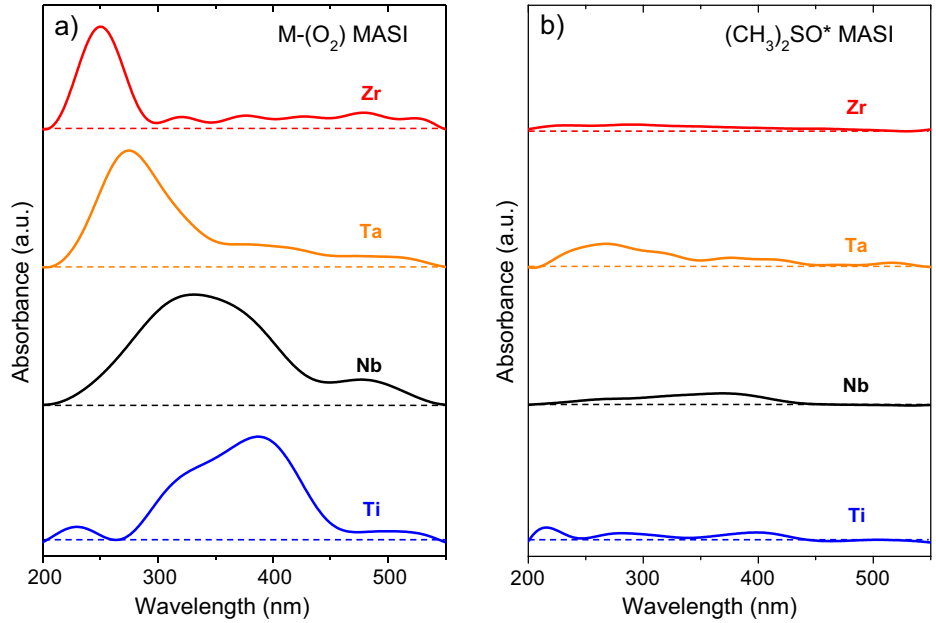

Fig. 5. Steady-state UV–vis spectra (solid lines) obtained in situ at conditions that generate (a) M-(O_2) saturated surfaces on Ti-BEA (blue; 0.7 mM C_6H_8S, 0.01 M H_2O_2), Nb-BEA (black; 7 mM C_6H_8S, 0.01 M H_2O_2), Ta-BEA (orange; 7 mM C_6H_8S, 0.01 M H_2O_2), and Zr-BEA (red; 5 mM C_6H_8S, 0.01 M H_2O_2); and at conditions that form (b) $(CH_3)_2SO$ saturated surfaces on Ti-BEA (blue; 5 mM $(CH_3)_2SO$, 0.01 M H_2O_2), Nb-BEA (black; 5 mM $(CH_3)_2SO$, 0.01 M H_2O_2), Ta-BEA (orange; 5 mM $(CH_3)_2SO$, 0.01 M H_2O_2), and Zr-BEA (red; 5 mM $(CH_3)_2SO$, 0.01 M H_2O_2). C_6H_8S was omitted from reaction solutions containing $(CH_3)_2SO$, because these solutions absorbed 300–500 nm light, which obscured features for M-(O_2) intermediates. Dashed lines represent baselines for each spectrum.

expected to produce M-(O_2) saturated surfaces (Fig. 5a) and low ratios that should form sulfoxide covered surfaces (Fig. 5b), as suggested by the interpretation of measured rates in Fig. 4 (Section 3.3). The UV–vis spectrum obtained in situ under conditions likely to produce a M-(O_2) saturated surface (Fig. 5a, 0.01 M H_2O_2, 0.7 mM C_6H_8S, 313 K, Ti-BEA) shows a complex absorbance feature between 300 and 420 nm, which is consistent with those of Ti-OOH and Ti-(η^2-O_2) species on Ti atoms grafted to mesoporous silicas [32,53,55,57] and within the framework of MFI [53,56,58] and BEA [30–32] zeolites. Alternatively, these UV–vis absorbance features are absent in the presence of $(CH_3)_2SO$ and H_2O_2 (Fig. 5b, 5 mM $(CH_3)_2SO$, 0.01 M H_2O_2, 313 K), which suggests that sulfoxides bind strongly to the Lewis acidic metal centers and prevent the activation of H_2O_2 to form M-(O_2). Notably, identical observations were made on all M-BEA, which corroborates the interpretation of measured rate dependencies on [H_2O_2] and [$(CH_3)_2SO$] (Fig. 4) that M-(O_2) and $(CH_3)_2SO^*$ become the MASI in the limits of low and high [C_6H_8S]:[H_2O_2], respectively (vide infra).

Oxidation turnover rates that decrease upon adding $(CH_3)_2SO$ and the displacement of reactive M-(O_2) intermediates by the sulfoxide imply that the identity and chemical nature of the solvent for ODS will influence rates of H_2O_2 activation and oxidation of thiophenes. Fig. 6 shows the turnover rates for C_6H_8S oxidation and the UV–vis absorbance intensities for Ti-(O_2) within six different solvent mixtures relevant for sulfoxidation catalysis [59–61] (note, all UV–vis spectra were obtained from a single Ti-BEA pellet to facilitate equitable comparisons). Among these solvents, sulfoxidation turnover rates are greatest in 10% v/v C_4H_8O in $C_{10}H_{22}$ ($9{\cdot}10^{-3}$ (mol C_6H_8SO) (mol Ti · s)$^{-1}$) and CH_3CN ($7{\cdot}10^{-3}$ (mol C_6H_8SO) (mol Ti · s)$^{-1}$), in part, because both these solvents allow for the formation of M-(O_2) saturated active sites as demonstrated by the intensity of the UV–Vis feature for M-(O_2) species (Fig. 6; 0.01 M H_2O_2, 313 K). These observations, together with the rate

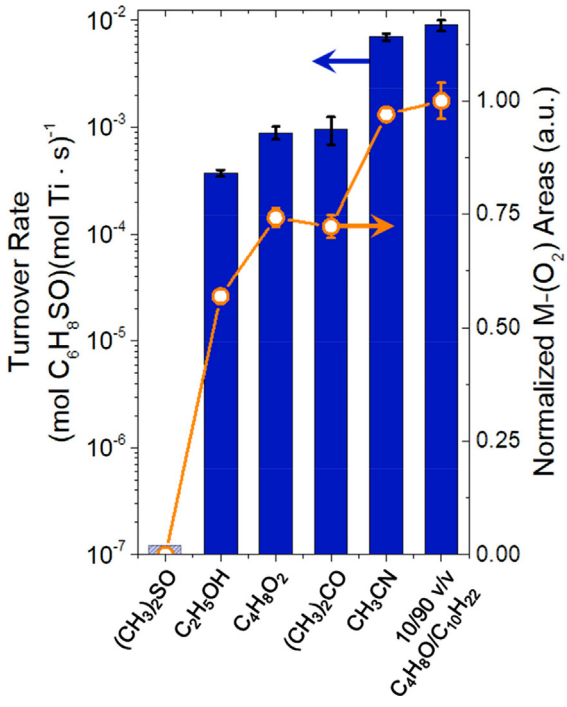

Fig. 6. Turnover rates (bars; 0.01 M C_6H_8S, 0.01 M H_2O_2, 313 K)) and UV–vis absorbance feature areas (○, for Ti-OOH and Ti-(η^2-O_2) intermediates, obtained in situ; 0.01 M H_2O_2, 313 K) for the oxidation of C_6H_8S as a function of solvent over Ti-BEA. The transparent bar for $(CH_3)_2SO$ represents that no measurable rate of C_6H_8S could be detected. For clarity, 10/90 v/v $C_4H_8O/C_{10}H_{22}$ represents 10%, by volume, of tetrahydrofuran in decane.

dependencies shown in Fig. 4, demonstrate that these solvent molecules do not effectively compete for Lewis acidic metal centers during catalysis. Turnover rates for C_6H_8S oxidation are significantly lower in oxygenated solvents (e.g., acetone ($(CH_3)_2CO$), *p*-dioxane ($C_4H_8O_2$), and ethanol (C_2H_5OH)), and become nearly immeasurable in $(CH_3)_2SO$. In addition, small amounts of dimethylsulfone ($(CH_3)_2SO_2$) formed when the solvent was $(CH_3)_2SO$, which correspond to a turnover rate of $5{\cdot}10^{-6}$ (mol $(CH_3)_2SO_2$) (mol Ti · s)$^{-1}$. The UV–vis spectra of M-(O_2) surface intermediates obtained for this series of solvents show a concomitant decrease in the peak areas for M-(O_2) absorbance features with the decrease in the turnover rates for sulfoxidation, which further suggests that these Lewis basic solvents competitively adsorb and displace reactive intermediates from the Lewis acidic Ti sites. Specifically, the strong Lewis basicity of O-atom lone pairs within the oxygenated solvents rivals that of H_2O_2, and together with the greater concentrations of the solvent molecules, leads to the saturation of Lewis acidic Ti metal centers by solvent molecules. The decrease in Ti-(O_2) coverage (taken to be proportional to the UV–vis absorbance feature area) does not change quantitatively with the differences in reaction rates in Fig. 6, which is apparent when comparing measurements with CH_3CN and C_2H_5OH. This disparity suggests, unsurprisingly, that solvents play a role beyond simple site competition and may change activation barriers for sulfoxidations either by changing the stability of transition states for oxidation of the sulfide moiety or by influencing the enthalpic cost to generate unoccupied active sites that subsequently bind and activate H_2O_2 within the catalytic cycle [62]. These energetic penalties result in an increase in the apparent activation barriers, which contribute to the large discrepancies in turnover rates that cannot be explained simply by competitive adsorption changing the surface coverage of M-(O_2) intermediates.

Quantitative comparisons of the nucleophilicity of small molecules were proposed by Mayr and co-workers based upon changes in first order rate constants for Friedel-Crafts aromatic substitutions that accompany differences in the electrophilicity of a complementary substrate (e.g., substitution of a phenyl-ring substitution) [63–65]. Mayr showed that the first-order rate constants for the solvolysis of benzylhydrinium salts (by varying phenyl-ring substitution to vary the electrophilicity) depend strongly on the structure and mole fraction (for binary mixtures) of the solvent, which are used to calculate the solvent nucleophilicity parameter (N_1) [65]. Establishing the functional dependence of sulfoxidation turnover rates on N_1 using a select subset of solvents provides one method to show rates for C_6H_8S oxidation depend on the Lewis basicity of solvent molecules and, potentially, to predict rates in untested solvent mixtures.

Fig. 7 shows turnover rates for the formation of C_6H_8SO on Ti-BEA as a function of N_1 for solvents and solvent mixtures relevant to ODS processes (0.01 M C_6H_8S, 0.01 M H_2O_2, 313 K). Turnover rates decrease exponentially with increasing values of N_1, which supports the hypothesis that these Lewis basic solvents competitively adsorb to the catalyst active sites and reduce rates of thiophene oxidation. This dependence also describes binary solvent mixtures (e.g., 50/50 and 10/90 v/v mixtures of CH_3OH and CH_3CN). Importantly, these comparisons seem useful to connect reports for H_2O_2-mediated oxidation catalysis on similar Lewis acid active sites (e.g., sulfoxidation, epoxidations, alcohol dehydrogenations). For example, alkene epoxidations are commonly performed within CH_3CN in academic studies [31,47,55,66], whereas, industrial processes often utilize other solvents (e.g., methanol for the epoxidation of propylene [67]). The correlation shown in Fig. 7 suggests that other liquid-phase oxidation reactions in an untested solvent or solvent mixture may be predicted semi-quantitatively using known values of N_1 and the volumetric ratio of the solvent components.

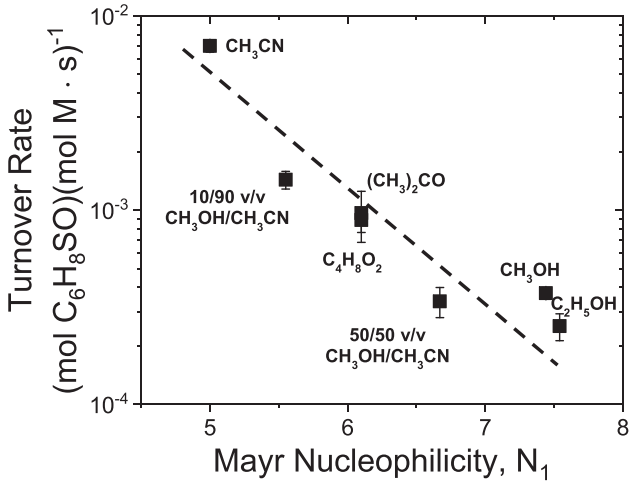

Fig. 7. Turnover rates for the oxidation of C_6H_8S as a function of N_1 over Ti-BEA (0.01 M C_6H_8S, 0.01 M H_2O_2, 313 K). For clarity, 50/50 v/v CH_3OH/CH_3CN represents an equi-volume mixture of CH_3OH and CH_3CN. The dashed line is intended to guide the eye.

3.5. Influence of the electron affinity of active sites on oxidation rates and selectivities

Transition state theory (TST) provides a foundation to quantify the differences in stability (e.g., free energy or enthalpy) between a reference state and a transition state for C_6H_8S oxidation or H_2O_2 decomposition [62]. Meaningful comparisons can be made between activation barriers for M-BEA catalysts to probe how the metal identity and electronic properties of the active site influence catalysis, provided that these measurements involve comparable references states (e.g., an M-(O_2) MASI). The application of TST assumes that the state immediately preceding the transition state and the transition state are in equilibrium, which is expressed as

$$M-(O_2)+C_6H_8S \overset{K^{\ddagger}_{Ox}}{\rightleftharpoons} M-(O_2)-C_6H_8S^{\ddagger} \quad (9)$$

where M-(O_2)-$C_6H_8S^{\ddagger}$ and $K^{\ddagger}_{Ox}$ represent the transition states and transition state equilibrium constants for C_6H_8S oxidation, respectively. The rates for C_6H_8S oxidation can then be expressed in terms of the numbers of transition states, resulting in

$$\frac{r_{Ox}}{[L]}=\frac{k_bT}{h}[M-(O_2)-C_6H_8S^{\ddagger}] \quad (10)$$

where T is the absolute temperature in Kelvin, and k_b and h are Boltzmann's and Planck's constants, respectively. Measurement of the reaction rates under a M-(O_2) MASI allows Eq. (10) to be combined with Eq. (6) to be re-expressed as

$$\frac{r_{Ox}}{[L]}=\frac{k_bT}{h}K^{\ddagger}_{Ox}[C_6H_8S] \quad (11)$$

which allows for $K^{\ddagger}_{Ox}$ to be determined by measurement of turnover rates for each reaction pathway at a given temperature. A comparable derivation is performed for H_2O_2 decomposition in the Supporting Information (section S5.2). Activation enthalpies ($\Delta H^{\ddagger}$) for both C_6H_8S oxidation and H_2O_2 decomposition are determined by regression of measured $K^{\ddagger}$ ($K^{\ddagger}_{Ox}$ and $K^{\ddagger}_{Dec}$ (i.e., for H_2O_2 decomposition)) for these pathways as functions of inverse temperature (Fig. S7) using the Eyring equation [62].

Table 2 shows the activation enthalpies for C_6H_8S oxidation ($\Delta H^{\ddagger}_{Ox}$) and H_2O_2 decomposition ($\Delta H^{\ddagger}_{Dec}$) measured at reaction conditions that produce M-(O_2) as the MASI on all M-BEA [68]. Table 2

Table 2
Activation enthalpies for C_6H_8S oxidation ($\Delta H^{\ddagger}_{Ox}$) and H_2O_2 decomposition ($\Delta H^{\ddagger}_{Dec}$) over M-BEA catalysts measured on M-(O_2) saturated surfaces.[a]

Sample	$\Delta H^{\ddagger}_{Ox}$ (kJ mol^{-1})	$\Delta H^{\ddagger}_{Dec}$ (kJ mol^{-1})
Ti-BEA	36 ± 3	31 ± 10
Nb-BEA	50 ± 5	45 ± 5
Ta-BEA	57 ± 6	56 ± 5
Zr-BEA	62 ± 4	65 ± 8

[a] $\Delta H^{\ddagger}_{Dec}$ and $\Delta S^{\ddagger}_{Dec}$ values for M-BEA under relevant conditions were taken from Ref. [29].

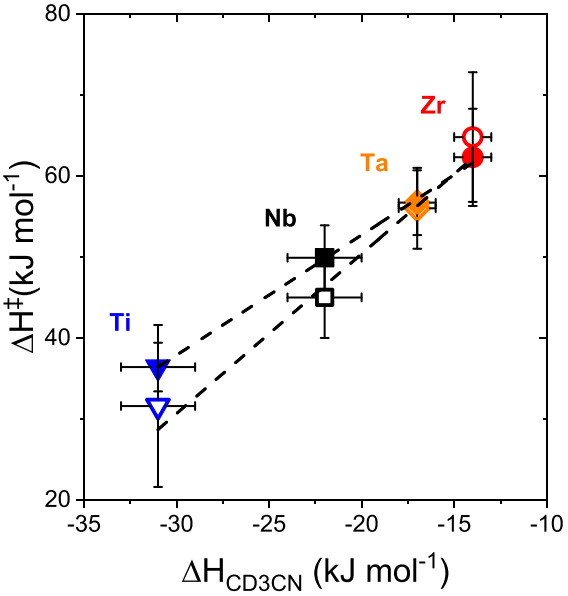

Fig. 8. Activation enthalpies for C_6H_8S oxidation (closed symbols) and H_2O_2 decomposition (open symbols) measured on M-(O_2) saturated active sites as a function of ΔH_{CD_3CN} coordinated to Lewis acid sites in Ti- (▼, ▽), Nb- (■, □), Ta- (◆, ◇), and Zr-BEA (●, ○). Dashed lines represent linear fits to the two sets of data.

shows that the differences in $\Delta H^{\ddagger}_{Ox}$ are consistent with the differences between sulfoxidation turnover rates across the M-BEA catalysts (Figs. 3 and 4). For example, the $\Delta H^{\ddagger}_{Ox}$ over Ti-BEA is 26 kJ mol^{-1} lower than Zr-BEA, which is consistent with the $3.5{\cdot}10^4$-fold greater turnover rate on Ti-BEA compared to Zr-BEA (Fig. 4).

Fig. 8 shows that values of $\Delta H^{\ddagger}_{Ox}$ and $\Delta H^{\ddagger}_{Dec}$ depend linearly on the enthalpy of adsorption for CD_3CN (ΔH_{CD_3CN}) among the M-BEA catalysts [69]. The values of ΔH_{CD_3CN} (Table 1) coordinated to Lewis acid sites provide quantitative measures of the electron affinity of the transition metal ion that constitutes the active site as it exists within the M-BEA framework. The linear correlation in Fig. 8 strongly suggests that the metal atoms that have greater electron affinities (i.e., "stronger" Lewis acids) present lower barriers for oxidation of thiophenes and therefore give greater turnover rates. These trends resemble those for alkene epoxidation, where M-BEA catalysts with larger ΔH_{CD_3CN} possess higher turnover rates and H_2O_2 selectivities for olefin epoxidation [31,32]. Interestingly, $\Delta H^{\ddagger}_{Ox}$ and $\Delta H^{\ddagger}_{Dec}$ depend less strongly on ΔH_{CD_3CN} (slope of ~1.5 and 1.9, respectively) than the activation enthalpies for cyclohexene [31] and styrene [32] epoxidation, which both possess a slope of ~3 when active sites are saturated with M-(O_2) intermediates. These comparisons suggest that the transition states for C_6H_8S oxidation involve less electron withdrawal from the M-(O_2) intermediate than those for alkene epoxidations. Collectively, these differences in the functional dependence of $\Delta H^{\ddagger}$ values on the electron affinity of the active sites appear consistent with the Lewis acid-base interactions contained within plausible transition state complexes, in which the

electron-rich functions of the reactant (i.e., lone pairs on the S-atom of thiophene or on the O-atoms of H_2O_2, or the C=C in alkenes) interact with the electron-deficient M-(O_2) intermediate. Chemical intuition suggests that the lone pairs on S- and O-atoms possess similarities and have greater electron densities than the C=C in alkenes. These M-BEA do not possess significant differences in the productive use of H_2O_2 (Fig. 4), which is explained by the similar values and dependencies of $\Delta H^{\ddagger}_{Ox}$ and $\Delta H^{\ddagger}_{Dec}$ on ΔH_{CD3CN} (Fig. 8). A possible explanation for this is that the M-(O_2) intermediates upon C_6H_8S oxidation or H_2O_2 decomposition must react with the lone pair of a S or O atom, respectively, which likely exchange charge and form bonds with M-(O_2) intermediates in similar ways.

4. Conclusions

Group 4 (Ti and Zr) and 5 (Nb and Ta) atoms substituted into the *BEA zeolite framework (M-BEA) irreversibly activate H_2O_2 to form pools of metal- hydroperoxide (M-OOH) and peroxide (M-(η^2-O_2)) intermediates that are critical for oxidative desulfurization (ODS) processes. These M-OOH and M-(η^2-O_2) surface species oxidize C_6H_8S (a representative thiophene) to form C_6H_8SO, which is then oxidized at much lower rates to form C_6HSO_2 by oxidative dearomatization. Interpretation of measured reaction kinetics, in conjunction with in situ UV–vis spectroscopy, show that C_6H_8S oxidation occurs through sets of elementary steps which have equivalent kinetic relevance on all M-BEA. Moreover, these steps and the derived oxidation rate expressions closely resemble those for cyclohexene and styrene epoxidations with H_2O_2 on these materials. Rates of sulfoxidation vary by several orders of magnitude across the series of M-BEA catalysts, however, the selectivities for H_2O_2 towards thiophene oxidation are relatively constant. Activation enthalpies for C_6H_8S oxidation and H_2O_2 decomposition are similar on each catalyst when M-(O_2) species dominate surfaces, which shows that both reaction pathways are equally sensitive to changes in the electron affinity (i.e., Lewis acidity) of the active sites that are quantified by differences in the enthalpy for adsorption of acetonitrile to these same sites. These comparisons indicate that the lone pairs on both the C_6H_8S and H_2O_2 interact in a similar fashion with the reactive intermediates such that the most "Lewis acidic" catalyst (i.e., Ti-BEA) results in the highest rates without sacrificing H_2O_2 selectivity.

The use of coordinating solvents has a great effect on sulfoxidation rates due to competitive adsorption to the active sites. Thiophene consumption rates decrease exponentially with the Mayr solvent nucleophilicity (N_1), which indicates that sulfoxidation rates in unknown solvents or solvent mixtures may be predicted by a quantifiable property of the reaction media. Interpretation of UV–vis spectra collected in situ during experiments that utilize solvents with varying values of N_1 shows that these changes are due, in part, to competitive adsorption of solvent molecules to active sites and the concomitant decrease in turnover rates. Collectively, this work reveals that turnover rates for sulfoxidation are maximized when highly electrophilic active sites (i.e., stronger Lewis acids) are combined with non-coordinating (i.e., weaker Lewis bases) solvents, which may guide the design of next-generation catalytic systems for sulfide oxidation.

Acknowledgements

We thank Ms. Zeynep Ayla for proofreading and editing this manuscript, Ms. Katherine Nagode for technical assistance, and Dr. Damien Guironnet for use of lab equipment to synthesize Ti-BEA. DTB was supported by the Department of Defense (DoD) through the National Defense, Science, and Engineering Graduate (NDSEG) Fellowship Program. This work was carried out, in part, in the Frederick Seitz Materials Research Laboratory Central Research Facilities at the University of Illinois. This work was supported by the U.S. Army Research Office under grant numbers W911NF-16-1-0128 and W911NF-18-1-0100.

References

[1] B. Obama, The irreversible momentum of clean energy, Science 355 (2017) 126–130.
[2] Y.E. Corilo, S.M. Rowland, R.P. Rodgers, Calculation of the total sulfur content in crude oils by positive-ion atmospheric pressure photoionization Fourier transform ion cyclotron resonance mass spectrometry, Energy Fuels 30 (2016) 3962–3966.
[3] Transport Policy US: Fuels: Diesel and Gasoline <http://www.transportpolicy.net/standard/us-fuels-diesel-and-gasoline/> (accessed January 16, 2018).
[4] G. Blanco-Brieva, J.M. Campos-Martin, S.M. Al-Zahrani, J.L.G. Fierro, Effectiveness of metal–organic frameworks for removal of refractory organosulfur compound present in liquid fuels, Fuel 90 (2011) 190–197.
[5] C.N. Lyles, D.F. Aktas, K.E. Duncan, A.V. Callaghan, B.S. Stevenson, J.M. Suflita, Impact of organosulfur content on diesel fuel stability and implications for carbon steel corrosion, Environ. Sci. Technol. 47 (2013) 6052–6062.
[6] J. Oudar, Sulfur adsorption and poisoning of metallic catalysts, Catal. Rev. 22 (2006) 171–195.
[7] R. Prins, V.H.J. De Beer, G.A. Somorjai, Structure and function of the catalyst and the promoter in Co—Mo hydrodesulfurization catalysts, Catal. Rev. 31 (1989) 1–41.
[8] H. Wang, E. Iglesia, Thiophene hydrodesulfurization catalysis on supported Ru clusters: Mechanism and site requirements for hydrogenation and desulfurization pathways, J. Catal. 273 (2010) 245–256.
[9] H. Wang, E. Iglesia, Mechanism and site requirements of thiophene hydrodesulfurization catalyzed by supported Pt clusters, ChemCatChem 3 (2011) 1166–1175.
[10] S. Oyama, Y. Lee, The active site of nickel phosphide catalysts for the hydrodesulfurization of 4,6- DMDBT, J. Catal. 258 (2008) 393–400.
[11] E. Rodriguez, W.S. Harvey, E.J. Ásbjörnsson, Review of H_2S Abatement Methods in Geothermal Plants, Thirty-Eighth Workshop on Geothermal Reservoir Engineering, Stanford University, Stanford, California, 2014.
[12] T. Song, Z. Zhang, J. Chen, Z. Ring, H. Yang, Y. Zheng, Effect of aromatics on deep hydrodesulfurization of dibenzothiophene and 4.6-dimethyldibenzothiophene over NiMo/Al_2O_3 catalyst, Energy Fuels 20 (2006) 2344–2349.
[13] B.C. Gates, H. Topsøe, Reactivities in deep catalytic hydrodesulfurization: challenges, opportunities, and the importance of 4-methyldibenzothiophene and 4,6- dimethyldibenzothiophene, Polyhedron 16 (1997) 3213–3217.
[14] H. Guo, Y. Sun, R. Prins, Hydrodesulfurization of 4,6-dimethyldibenzothiophene over Pt supported on γ-Al2O3, SBA-15, and HZSM-5, Catal. Today 130 (2008) 249–253.
[15] X. Rozanska, R.A. van Santa, F. Hutschka, J. Hafner, A periodic density functional theory study of thiophenic derivative cracking catalyzed by mordenite, J. Catal. 215 (2003) 20–29.
[16] N.M. Wilson, D.T. Bregante, P. Priyadarshini, D.W. Flaherty, Production and use of H_2O_2 for atom-efficient functionalization of hydrocarbons and small molecules, Catalysis 29 (2017) 122–212.
[17] G.W. Wagner, P.W. Bartram, L.R. Procell, D.C. Sorrick, V.D. Henderson, A.L. Turetsky, V.K. Rastogi, Y.-C. Yang, Decon Green™: Development and chemical biological agent efficacy testing, U.S. Army Research, Development and Engineering Command, Aberdeen Proving Ground, MD, 2004.
[18] L. Kong, G. Li, X. Wang, B. Qu, Oxidative desulfurization of organic sulfur in gasoline over Ag/TS-1, Energy Fuels 20 (2006) 896–902.
[19] L. Kong, G. Li, X. Wang, Mild oxidation of thiophene over TS-1/H_2O_2, Catal. Today 93–95 (2004) 341–345.
[20] Q. Du, Y. Guo, H. Duan, H. Li, Y. Chen, H. Liu, Synthesis of hierarchical TS-1 zeolite via a novel three-step crystallization method and its excellent catalytic performance in oxidative desulfurization, Fuel 188 (2017) 232–238.
[21] A. Corma, M. Iglesias, F. Sánchez, Large pore Ti-zeolites and mesoporous Ti-silicalites as catalysts for selective oxidation of organic sulfides, Catal. Lett. 39 (1996) 153–156.
[22] A. Bazyari, A.A. Khodadadi, A. Haghighat Mamaghani, J. Beheshtian, L.T. Thompson, Y. Mortazavi, Microporous titania–silica nanocomposite catalyst-adsorbent for ultra-deep oxidative desulfurization, Appl. Catal. B 180 (2016) 65–77.
[23] A.M. Cojocariu, P.H. Mutin, E. Dumitriu, F. Fajula, A. Vioux, V. Hulea, Non-hydrolytic synthesis of mesoporous silica-titania catalysts for the mild oxidation of sulfur compounds with hydrogen peroxide, Chem. Commun. 5357–5359 (2008).
[24] N.E. Thornburg, J.M. Notestein, Rate and selectivity control in thioether and alkene oxidation with H_2O_2 over phosphonate-modified niobium(V)-silica catalysts, ChemCatChem 9 (2017) 3714–3724.
[25] V. Hulea, F. Fajula, J. Bousquet, Mild oxidation with H_2O_2 over Ti-containing molecular sieves – A very efficient method for removing aromatic sulfur compounds from fuels, J. Catal. 198 (2001) 179–186.
[26] P. Moreau, V. Hulea, S. Gomez, D. Brunel, F. Di Renzo, Oxidation of sulfoxides to sulfones by hydrogen peroxide over Ti-containing zeolites, Applied Catalysis A 155 (1997) 253–263.
[27] L. Nemeth, S.R. Bare, W. Rathbun, M. Gatter, J. Low, Oxidative desulfurization of sulfur compounds: Oxidation of thiophene and derivatives with hydrogen peroxide using Ti-Beta catalyst, Stud. Surf. Sci. Catal. 174 (2008) 1017–1020.

[28] A. Chica, A. Corma, M. Domine, Catalytic oxidative desulfurization (ODS) of diesel fuel on a continuous fixed-bed reactor, J. Catal. 242 (2006) 299–308.
[29] J.M. Fraile, C. Gil, J.A. Mayoral, B. Muel, L. Roldán, E. Vispe, S. Calderón, F. Puente, Heterogeneous titanium catalysts for oxidation of dibenzothiophene in hydrocarbon solutions with hydrogen peroxide: On the road to oxidative desulfurization, Appl. Catal. B 180 (2016) 680–686.
[30] D.T. Bregante, P. Priyadarshini, D.W. Flaherty, Kinetic and spectroscopic evidence for reaction pathways and intermediates for olefin epoxidation on Nb in * BEA, J. Catal. 348 (2017) 75–89.
[31] D.T. Bregante, D.W. Flaherty, Periodic trends in olefin epoxidation over group IV and V framework substituted zeolite catalysts: a kinetic and spectroscopic study, J. Am. Chem. Soc. 139 (2017) 6888–6898.
[32] D.T. Bregante, N.E. Thornburg, J.M. Notestein, D.W. Flaherty, Consequences of confinement for alkene epoxidation with hydrogen peroxide on highly dispersed group 4 and 5 metal oxide catalysts, ACS Catal. 8 (2018) 2995–3010.
[33] N.E. Thornburg, S.L. Nauert, A.B. Thompson, J.M. Notestein, Synthesis-structure-function relationships of silica-supported niobium(V) catalysts for alkene epoxidation with H_2O_2, ACS Catal. 6 (2016) 6124–6134.
[34] S. Dzwigaj, Y. Millot, M. Che, Ta(V)-single site BEA zeolite by two-step postsynthesis method: Preparation and characterization, Catal. Lett. 135 (2010) 169–174.
[35] S. Dzwigaj, Y. Millot, C. Méthivier, M. Che, Incorporation of Nb(V) into BEA zeolite investigated by XRD, NMR, IR, DR UV–vis, and XPS, Microporous Mesoporous Mater. 130 (2010) 162–166.
[36] B. Tang, W. Dai, X. Sun, N. Guan, L. Li, M. Hunger, A procedure for the preparation of Ti-Beta zeolites for catalytic epoxidation with hydrogen peroxide, Green Chem. 16 (2014) 2281–2291.
[37] P. Wolf, C. Hammond, S. Conrad, I. Hermans, Post-synthetic preparation of Sn-Ti- and Zr-beta: a facile route to water tolerant, highly active Lewis acidic zeolites, Dalton Trans. 43 (2014) 4514–4519.
[38] J. Wang, V.F. Kispersky, N.W. Delgass, F.H. Ribeiro, Determination of the Au active site and surface active species via operando transmission FTIR and isotopic transient experiments on 2.3wt.% Au/TiO_2 for the WGS reaction, J. Catal. 289 (2012) 171–178.
[39] R.J. Madon, M. Boudart, Experimental criterion for the absence of artifacts in the measurement of rates of heterogeneous catalytic reactions, Ind. Eng. Chem. Fundam. 21 (1982) 438–447.
[40] J.W. Harris, M.J. Cordon, J.R. Di Iorio, J.C. Vega-Vila, F.H. Ribeiro, R. Gounder, Titration and quantification of open and closed Lewis acid sites in Sn-Beta zeolites that catalyze glucose isomerization, J. Catal. 335 (2016) 141–154.
[41] R. Hajjar, Y. Millot, P.P. Man, M. Che, S. Dzwigaj, Two kinds of framework Al sites studied in BEA zeolite by X-ray diffraction, Fourier transform infrared spectroscopy, NMR techniques, and V probe, J. Phys. Chem. C 112 (2008) 20167–20175.
[42] Y. Oumi, K. Matsuba, M. Kubo, T. Inui, A. Miyamoto, Selective T-site substitution as a cause of the anisotropy of lattice expansion in titanoscilicate-1 investigated by molecular dynamics and computer graphics, Microporous Mater. 4 (1995) 53–57.
[43] B.D. Cullity, S.R. Stock, Elements of X-ray Diffraction, Pearson, United Kingdom, 2001.
[44] Samples of M-BEA with high loadings were necessary to visualize the shift in 2θ, because the low loading used for as not enough silanol nests were substituted within the M-BEA with lower metal loadings (Table 1).
[45] B. Tang, W. Dai, G. Wu, N. Guan, L. Li, M. Hunger, Improved postsynthesis strategy to Sn-beta zeolites as lewis acid catalysts for the ring-opening hydration of epoxides, ACS Catal. 4 (2014) 2801–2810.
[46] J. Klaas, G. Schulz-Ekloff, N.I. Jaeger, UV-visible diffuse reflectance spectroscopy of zeolite-hosted mononuclear titanium oxide species, J. Phys. Chem. B 101 (1997) 1305–1311.
[47] N.E. Thornburg, A.B. Thompson, J.M. Notestein, Periodic trends in highly dispersed groups IV and V supported metal oxide catalysts for alkene epoxidation with H_2O_2, ACS Catal. 5 (2015) 5077–5088.
[48] W. Daniell, N.Y. Topsøe, H. Knözinger, An FTIR study of the surface acidity of USY zeolites: Comparison of CO, CD3CN, and C5H5N probe molecules, Langmuir 17 (2001) 6233–6239.
[49] W. Al-Maksoud, S. Daniele, A.B. Sorokin, Practical oxidation of sulfides to sulfones by H_2O_2 catalysed by titanium catalyst, Green Chem. 10 (2008) 447.
[50] E.V. Anslyn, D.A. Dougherty, Modern Physical Organic Chemistry, University Science, 2005.
[51] J.L. Holmes, C. Aubry, Group additivity values for estimating the enthalpy of formation of organic compounds: an update and reappraisal. 2. C, H, N, O, S, and halogens, J. Phys. Chem. A 116 (2012) 7196–7209.
[52] Dimethylsulfoxide was used a surrogate for 2,5-dimethylthiophene oxide, as sufficiently pure samples of 2,5-dimethylthiophene oxide were not obtainable.
[53] C.W. Yoon, K.F. Hirsekorn, M.L. Neidig, X. Yang, T.D. Tilley, Mechanism of the decomposition of aqueous hydrogen peroxide over heterogeneous TiSBA15 and TS-1 selective oxidation catalysts: insights from spectroscopic and density functional theory studies, ACS Catal. 1 (2011) 1665–1678.
[54] At differential conversion, [C6H8SO] is very small, which results in a very small value of k7[C6H8SO].
[55] D.A. Ruddy, T.D. Tilley, Kinetics and mechanism of olefin epoxidation with aqueous H_2O_2 and a highly selective surface-modified TaSBA15 heterogeneous catalyst, J. Am. Chem. Soc. 130 (2008) 11088–11096.
[56] F. Bonino, A. Damin, G. Ricchiardi, M. Ricci, G. Spanó, R. D'Aloisio, A. Zecchina, C. Lamberti, C. Prestipino, S. Bordiga, Ti-peroxo species in the TS-1/H_2O_2/H_2O system, J. Phys. Chem. B 108 (2004) 3573–3583.
[57] I.D. Ivanchikova, I.Y. Skobelev, N.V. Maksimchuk, E.A. Paukshtis, M.V. Shashkov, O.A. Kholdeeva, Toward understanding the unusual reactivity of mesoporous niobium silicates in epoxidation of C=C bonds with hydrogen peroxide, J. Catal. 356 (2017) 85–99.
[58] S. Bordiga, E. Groppo, G. Agostini, J.A. van Bokhoven, C. Lamberti, Reactivity of surface species in heterogeneous catalysts probed by in situ X-ray absorption techniques, Chem. Rev. 113 (2013) 1736–1850.
[59] V. Hulea, P. Moreau, F.D. Renzo, Thioether oxidation by hydrogen peroxide using titanium-containing zeolites as catalysts, J. Mol. Catal. A: Chem. 111 (1996) 325–332.
[60] V. Hulea, P. Moreau, The solvent effect in the sulfoxidation of thioethers by hydrogen peroxide using Ti-containing zeolites as catalysts, J. Mol. Catal. A: Chem. 113 (1996) 499–505.
[61] B. Saito, T. Katsuki, Ti(salen)-catalyzed enantioselective sulfoxidation using hydrogen peroxide as a terminal oxidant, Tetrahedron Lett. 42 (2001) 3873–3876.
[62] I. Chorkendorff, J.W.H. Niemantsverdriet, Concepts of Modern Catalysis and Kinetics, 2nd ed., Wiley-VCH Verlag Gmbh & Co., Weinheim, 2007.
[63] H. Mayr, A.R. Ofial, Do general nucleophilicity scales exist?, J Phys. Org. Chem. 21 (2008) 584–595.
[64] H. Mayr, M. Patz, Scales of nucleophilicity and electrophilicity: A system for ordering polar organic and organometallic reactions, Angew. Chem. Int. Ed. 33 (1994) 938–957.
[65] S. Minegishi, S. Kobayashi, H. Mayr, Solvent nucleophilicity, J. Am. Chem. Soc. 126 (2004) 5174–5181.
[66] N. Morlanés, J.M. Notestein, Grafted Ta–calixarenes: Tunable, selective catalysts for direct olefin epoxidation with aqueous hydrogen peroxide, J. Catal. 275 (2010) 191–201.
[67] P. Bassler, H. Göbbel, M. Weidenbach, The new HPPO process for propylene oxide: From joint development to worldscale production, Chem. End. Trans. 21 (2010) 571–577.
[68] Under reaction conditions that result in surfaces saturated with M-(OOH) and M-(η2-O2) species, measured rates do not reflect processes for the activation of H2O2.
[69] Activation enthalpies and the turnover rates for a given M-BEA do not depend on the density of active sites for a given material, but rather depend solely on how the rates of sulfoxidation change with the varied reaction condition (e.g., temperature or solvent).